Temperature Dependant Mechanical Property Characterisation Using Digital Image Correlation and Infrared Thermography

Matthew Blackwell[a], Maxwell Vos[b], Sarah George[b], Melody Neaves[a], Thorsten Becker[b],

Abstract: *Accurate mechanical property charac-terisation of high-temperature high-performance materials, such as additively manufactured (AM) Inconel 718 (IN718), is crucial to ensure the reliability of components. A sud-den drop in strength accompanied by significant embrittle-ment occurs in wrought IN718 near* $700\,°C$*. It is not clear whether AM IN718 exhibits this behaviour. The high cost of these materials and manufacturing methods necessitate the development of specimen-efficient testing techniques that allow material properties to be extracted simultaneously over a range of testing conditions. This paper presents a test setup, which is used to determine high-temperature mechanical properties over a range of operating temperatures by integrating digital image correlation (DIC) and full-field infrared thermography (IR). A purpose-designed specimen is resistively heated using a Gleeble 3800 thermomechanical simulator to create a thermal gradient across the length of the specimen. A high-temperature DIC setup and IR camera are used to capture the specimen surface's displacement and full-field IR data. These datasets are temporally synchronised using a common triggering system and spatially correlated to allow for the extraction of temperature-dependent properties for a range of up to* $100\,°C$ *from a single tensile test. The setup is shown to successfully capture the strength drop-off and embrittlement of AM IN718.*

Additional keywords: Full-field, Digital Image Correlation, Infrared Thermography, High-Temperature, Inconel 718.

Abbreviations

AC	Air cooled
AM	Additively manufactured
CF	Correction factor
DIC	digital image correlation
IN718	Inconel 718
IR	Infrared
LPBF	Laser-powder bed fusion
PSD	particle size distribution
ROI	Region of interest
RT	Room temperature
UTS	Ultimate tensile strength
VHT	Very high temperature
WQ	Water quenched
%EL	Percentage elongation

[a] Department of Mechanical and Mechatronic Engineering, Stellenbosch University, Joubert street, Stellenbosch 7602, South Africa, Email. matthewrsacape@gmail.com

[b] Centre for Materials Engineering, University of Cape Town, Library Rd, Cape Town, 7701, South Africa

1 Introduction

A recent push towards carbon reduction has necessitated an increase in the fuel efficiency of commercial jet engines [1]. Higher efficiencies can be achieved by increasing engine operating temperatures; however, material capabilities often limit this. Designers have started incorporating cooling channels within parts to increase engine gas temperatures. The design of these cooling channels is limited in part by the ability to manoeuvre the tooling within the turbine blade. This plays into the strengths of AM materials since AM technologies allow for the layer-wise addition of material rather than the subtraction of material. This layer-wise manufacturing technique allows built-in cooling channels, along with other design complexities, to be created during the building of a part rather than being machined after a part is formed [2].

IN718 is a nickel-based superalloy with substantial strength retention at temperatures up to $650\,°C$ and excellent corrosion resistance, among other benefits. As such, it is widely employed in its wrought and cast forms in the aerospace industry and accounts for approximately 34 % of the total mass of jet turbine engines [3]. Heat treatments for wrought and cast IN718 are well established for high-temperature use, and the microstructure has been extensively studied. On the other hand, the high-temperature mechanical properties of IN718 produced by LPBF, an AM technique, are not well documented. Due to the unique microstructure of LPBF materials, it is not possible to assume that the LPBF produced material will exhibit the same properties as the conventionally produced IN718.

Accurate characterisation of the high-temperature mechanical behaviour of LPBF IN718 is crucial to ensure the reliability and performance of the components. One notable material behaviour of wrought IN718 is a sudden drop in strength near $700\,°C$ [4], accompanied by embrittlement of the material between $650\,°C$ to $800\,°C$ [5]. It is unclear whether LPBF IN718 will exhibit a similar strength drop and embrittlement under the same conditions. Moreover, the high cost of these materials and manufacturing methods necessitates the development of specimen-efficient testing techniques that allow material properties to be extracted simultaneously in a range of testing conditions. Van Rooyen and Becker [6] experimented with the concept of measuring high-temperature mechanical prop-

erties of steel from a power plant with a non-uniform temperature achieved through resistive heating. This heating method was used with a combination of high-temperature DIC and IR to extract mechanical properties over a range of up to 120 °C from a single specimen. Their testing was limited to peak specimen temperatures of 600 °C. This paper presents an improved testing setup which incorporates automated temporal and spatial synchronisation of the data and applies the testing method to LPBF produced IN718.

2   Materials

The powder used for specimen manufacturing was gas atomised 15 μm to 53 μm IN718 powder manufactured by AP&C [7] with composition shown in Table 1. The PSD ranged between 21.25 μm to 51.64 μm (D_{10} – D_{90}).

Table 1   Elemental composition of IN718 powder* from AP&C [7]. *Only main constituent elements are presented, with the balance assumed to be Fe

Element	Ni	Cr	Nb+Ta	Mo	Ti	Al	Co	C
wt%	53.22	18.7	4.96	2.94	0.85	0.58	<0.1	0.04

Tensile specimens were built in cylindrical form in two orientations with the long axis either parallel or perpendicular to the build plate. A rectangular scan strategy was employed with the following machine settings: laser power of 190 W; laser spot size of approximately 70 μm; scan speed of 800 mm s^{-1}; hatch spacing of 120 μm; and powder layer thickness of 30 μm with a 45° scan offset and 90° scan path rotation between subsequent build layers. Printing was performed under an argon atmosphere with oxygen levels kept below 0.01 %. A stainless-steel build plate was used due to its ability to ensure strong metallurgical bonding and low cost of resurfacing between builds [8] and no build plate heating was applied. Two different heat treatment schemes, shown in Table 2, were applied after printing for comparative purposes. The stress relief was conducted while specimens were attached to the build plate.

Table 2   Heat treatment schemes applied to LPBF IN718 specimens in this research.

Designation	Stress relief	Homogenisation	Ageing
LPBF-H1110	950 °C for 2 h, AC to RT	1110 °C for 2 h, WQ to RT	720 °C for 24 h, AC to RT
LPBF-H1020	950 °C for 2 h, AC to RT	1020 °C for 1 h, WQ to RT	720 °C for 24 h, AC to RT

3   Test Setup

The test setup consists of three main interconnected elements. These elements, along with their relative physical positioning, are shown in Figure 1 and include the Gleeble 3800 thermo-mechanical simulator [9], stereo DIC system, and IR camera. The Gleeble performed two main functions during testing, namely displacement and temperature control, and thus took the role of both tensile machine and heating furnace. The electrical input used to heat the specimen was controlled via feed-

back from a K-type thermocouple spot welded to the specimen's top surface centred along the gauge region's length with an accuracy of ± 0.2 mm. Two additional thermocouples, each approximately 15 mm from the specimen centre, were welded to the specimen for IR image adjustment.
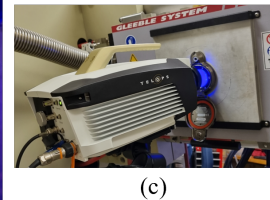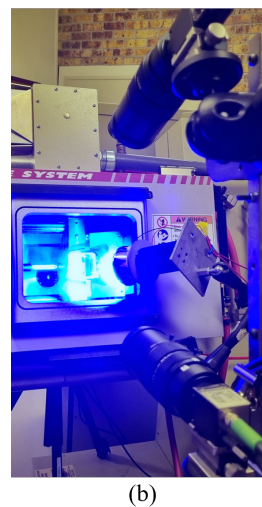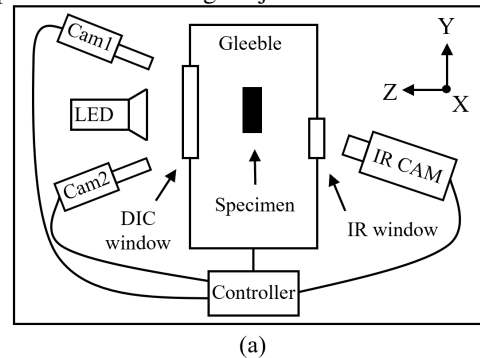

Figure 1   (a) The relative positioning of all major system elements. (b) DIC system positioned at the front of the Gleeble. (c) Positioning of the IR camera at the back of the Gleeble.

The measurement accuracy of the Gleeble thermal control system is 1 °C and therefore the thermal control accuracy was limited to that of the K-type thermocouple which is 0.75 % or 3.4 °C and 6.4 °C at 450 °C and 850 °C respectively. The Gleeble can apply a vacuum of below 0.5 torr within the testing chamber during testing. This was used to limit specimen oxidation, discolouration of the paint used to create the speckle pattern, and heat haze that would negatively impact the DIC measurements. The hydraulic ram, which was used to apply the load at a constant grip displacement rate, has a displacement accuracy of 0.01 mm and the fitted 100 kN load-cell had a calibrated accuracy of 0.01 kN.

The geometry of the tensile specimen, shown in Figure 2(a), was based on a design by van Rooyen and Becker [6] that was designed for use with resistive heating to provide a parabolic thermal profile along the length of the specimen. The reduced cross-section gauge region was lengthened to 40 mm, instead of 25 mm, to increase the surface area available for DIC strain averaging at each temperature. Figure 2(b) shows the loading and electrical paths applied using H13 tool steel grip extenders which were necessary to mitigate grips blocking the views of
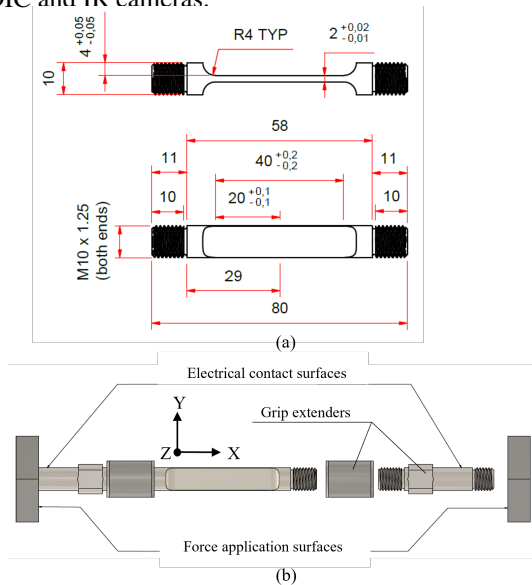
the DIC and IR cameras.

Figure 2   (a) Gleeble tensile specimen geometry (mm). (b) Partially exploded view of the tensile loading train including grip extenders showing locations of force and electrical contact and testing coordinate system.

A stereo DIC system was used for full-field displacement measurement through a borosilicate glass window on one side of the Gleeble. 75 mm double Gauss lenses were mounted to the cameras to achieve a suitable resolution. Narrow band-pass filters from Edmund Optics [10] were mounted on the lenses to avoid image saturation due to radiation emitted at higher temperatures. These filters have a central wavelength of 470 nm and a full-width half-maximum width of 85 nm which blocks most visible radiation emitted by the specimen at 850 °C. These filters significantly reduce the overall incident light to the sensor and were therefore paired with a focused blue-light LED with a peak wavelength of 451 nm and rated power of approximately 20 W. DIC hardware parameters are reported in Table 3 according to the iDICs guidelines [11].

Table 3   DIC hardware parameters reported according to iDICs guidelines [11]

Camera make and model	Baumer VCXU-50M
Image resolution	2448×2048 pixels
Lens manufacturer and model	Edmund Optics 75 mm double Gauss
Focal length	75 mm
Aperture	~ 18 f/
Field-of-view	~ 69.49 mm $\times 58.13$ mm
Image scale	~ 35.23 pixels mm^{-1}
Stereo angle	$\sim 22°$
Stand-off distance	~ 650 mm
Image acquisition rate	0.125 Hz
Patterning technique	Black speckles on top of white speckles (no solid background)
Pattern feature size	30 pixels

The speckle pattern consisted of both white and black speckles applied directly to the bare specimen surface rather than applying black speckles to a solid white paint background. This was found to improve paint adhesion during high strains.

Full-field IR measurement was achieved using a Telops FAST M350 [12] IR camera positioned at the back of the Gleeble. The IR camera captured images of the specimen's rear surface, which was painted with matte black VHT flame-proof paint [13] to provide constant emissivity across the entire surface and reduce reflections. The IR camera's measurable temperature range during testing was 133.7 °C to 1252.7 °C, with a thermal resolution of 20 mK, image resolution of 640×512 pixels and aperture of f/3. A Fluke ClirVu CV200 IR viewing window [14] was used for IR viewing access into the vacuum chamber.

4   Temporal Synchronisation, Spatial Calibration, and Testing Procedure

Temporal synchronisation was achieved during testing using a custom-built controller unit, which was designed around an Arduino Uno [15]. The controller unit was responsible for the simultaneous triggering of both DIC and IR systems at a preset acquisition rate. The controller unit was also responsible for saving and storing the synchronised data.

Both DIC and IR systems required spatial calibration to allow for overlay of the two datasets. To do this, the secondary DIC camera and IR camera needed to be spatially calibrated with respect to the first, master, DIC camera. To conduct a true calibration, all cameras need to face the same surface of the specimen. This was not possible due to space and IR window size limitations. For the purposes of this research, it was assumed that both specimen surfaces deformed equally during testing and therefore, an accurate calibration could still be achieved. Spatial calibration was achieved in the MatchID Calib DIC software (v2023.2.0) [16] using a custom calibration plate created by placing two similar calibration plates back-to-back. The calibration plate's front, DIC facing, surface was an ordinary single plane MatchID calibration plate seen in Figure 3(a). The back, IR camera-facing, surface of the calibration plate was machined from a plate of aluminium with holes corresponding to the MatchID calibration plate dots, as shown in Figure 3(b). The two faces of the calibration plate were then placed back-to-back and mounted on a stand to allow for two-axis rotation. A single calibration image was taken for the IR camera calibration with the calibration plate aligned with the specimen surface. Thereafter, images of the calibration plate were taken in various orientations for the stereo DIC calibration. In MATLAB (vR2022b) [17], the *imfindcircles*, *tform* and *imwarp* functions were used to identify corresponding dots on both calibration plates, calculate and apply the required transformation matrix to warp the IR image so that it would appear to be taken from the perspective of the second DIC camera, as shown in Figure 3(c). By doing this, the stereo calibration file that relates to the DIC cameras can also be used to relate to the IR camera.

After image calibration, the specimen was loaded into the Gleeble and a 400 N preload was applied to ensure strong electrical contact. A signal was sent from the Gleeble to trigger the controller to start image acquisition. Heating commenced
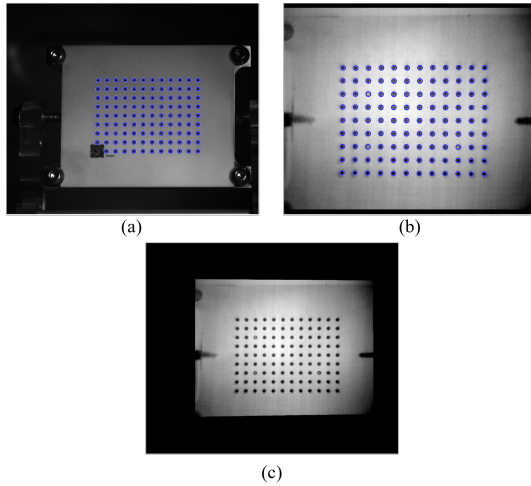
(a)

(b)

(c)

Figure 3 DIC camera 2 image of the front calibration plate with marker locations identified in MATLAB. (b) IR image of the back calibration plate with marker locations identified in MATLAB. (c) Warped IR image.

at a rate of $10\,^{\circ}\mathrm{C\,s}^{-1}$. The thermal profile was allowed to stabilise for ten minutes upon reaching the testing temperature. After the stabilisation period, the tensile test was automatically started by the Gleeble.

A constant displacement rate of $0.2\,\mathrm{mm\,min}^{-1}$ was chosen to meet quasi-static conditions, which equals a strain rate of $0.005 \pm 0.002\,\mathrm{mm\,mm}^{-1}\,\mathrm{min}^{-1}$. This meets the quasi-static strain rate requirements stipulated in ASTM-E21 [18] standard for high-temperature testing of metallic materials. Due to the uneven thermal gradient of the specimen, the effective strain rate increased to a maximum of 0.0054 mm/mm/min in the hottest region during plastic deformation. This increased strain rate is allowed in ASTM-E21.

5   Post Processing of Test Data

The RevealIR [12] IR camera software outputs data as a floating-point tagged image file format with pixel values corresponding to temperature values. The default temperature conversion formulas do not account for factors such as surface emissivity and transmissivity of mediums between the specimen and camera. These were corrected using measurements from the three thermocouples welded to the specimen using the correction factors (CF) in Equations 1 and 2.

$$IR_{\text{image, CF1}} = IR_{\text{image}} \times CF1(N_{\text{image}}) \tag{1}$$

$$
\begin{aligned}
IR_{\text{image, CF2}}(x_{\text{pixcolumn}}) = \\
IR_{\text{image, CF1}}(x_{\text{pixcolumn}}) \times CF2(x_{\text{pixcolumn}})
\end{aligned}
\tag{2}
$$

In these equations, $CF1$ corrected for the change in the emissivity caused by the degradation and darkening of the paint. As such, this correction factor was spatially constant but changed for each timestamp. This CF was calculated as the ratio of the IR and control thermocouple values for one image near the start of the test sequence and one image near the end of the test sequence. Intermediate CFs were determined by linear interpolation. $CF2$ corrected for the transmissivity of the IR viewing window. $CF2$ remained constant over time but

varied spatially. To account for this, the three thermocouple temperatures were used to calculate the CF for three locations along the length of the specimen. Quadratic interpolation was used to determine the correction for each pixel along the specimen length (along ($x_{\text{pixcolumn}}$) pixel vectors). The correction along the height of the sample was constant.

DIC analysis was performed on a single ROI which covered the entire specimen. Following this analysis, strain calculations were performed, and thermal images were imported. The thermal image overlay process was automated by MatchID using the DIC calibration file. The data sets were subsequently merged into a single data set and exported in matrix format for further analysis.
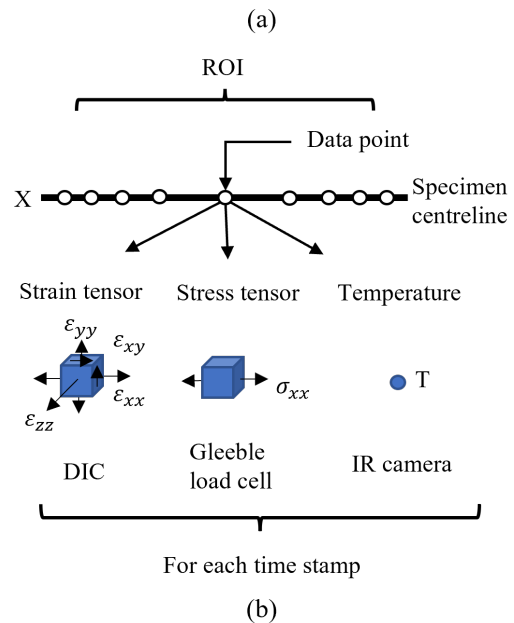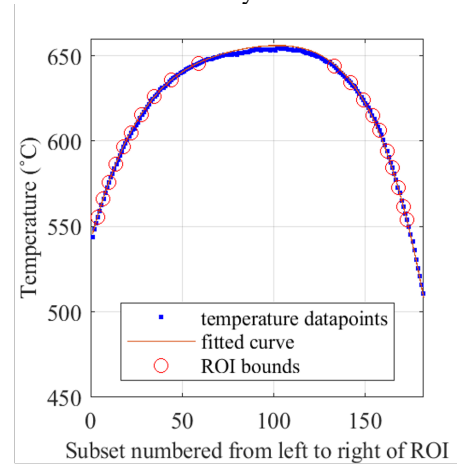

(a)

For each time stamp

(b)

Figure 4   (a) Thermal profile of a specimen at $650\,^{\circ}\mathrm{C}$ overlayed with data fit and sub-ROI bounds. (b) Overview of data components.

The last steps of the processing workflow, which were completed in MATLAB, were data cleanup and extraction of temperature-dependent mechanical properties. Data cropping was performed, followed by smoothing using the *smoothdata* function with *movmean* (moving mean method) selected. Thereafter, working from the specimen centre outwards in both directions, the data was subdivided into smaller sub-

ROIs, each approximating a span of 10 °C. This is shown in Figure 4(a), where the data points representing the sub-ROI bounds have been circled in red. In all subsequent operations, each sub-ROI was handled independently. The temperature was then averaged for each sub-ROI to give a single temperature representative of the sub-ROI. The strain for each sub-ROI at each time step was averaged to provide vectors, with each element corresponding to a time step.

Figure 4(b) shows a summary of the resulting data. After the ROI subdivision, a stress-strain curve was plotted for each sub-ROI and the yield strength and percentage elongation (%EL) were calculated. %EL was only calculated for the central sub-ROI at the highest temperature where the specimen failed.
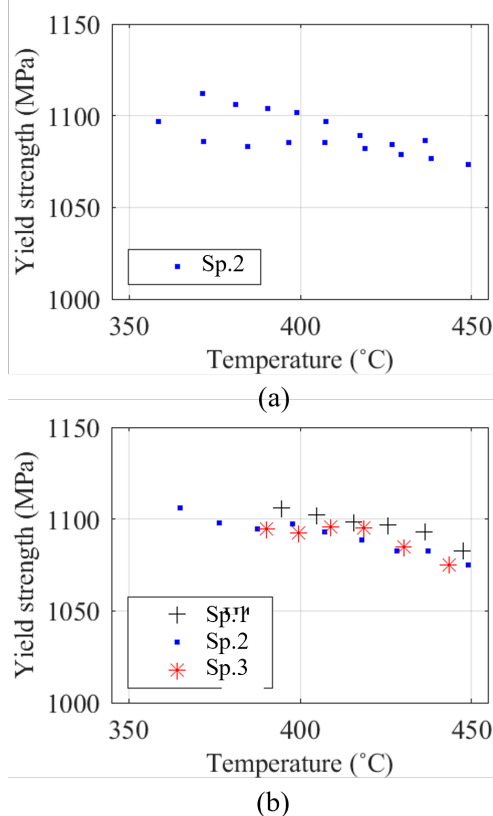

(a)

(b)

Figure 5 (a) YS data extracted from both halves of specimen 2 (Sp.2) subject to homogenisation at 1020 °C. (d) Comparative yield data after averaging the two specimen halves of three different tests.

6 Results

Figure 5(a) shows the yield strength results from the two halves of a single specimen. The data shows a close correlation between the two halves of each specimen as can be seen by the tight grouping of yield strength values at each temperature. Figure 5(b) shows the yield results of three specimens after averaging the results from both halves of each specimen. The data suggest excellent repeatability and consistency of both the manufacturing and testing methods with a variation of less than 15 MPa in yield strength between specimens.

Figure 6 shows the trends in yield strength and ductility as

a function of temperature for the two different heat treatments and two print orientations. In Figure 6(a), it is observed that all LPBF IN718 specimens exhibit the same rapid strength decrease that is seen in wrought IN718 starting around 650 °C. The rate of strength decrease is roughly the same regardless of heat treatment and print orientation.
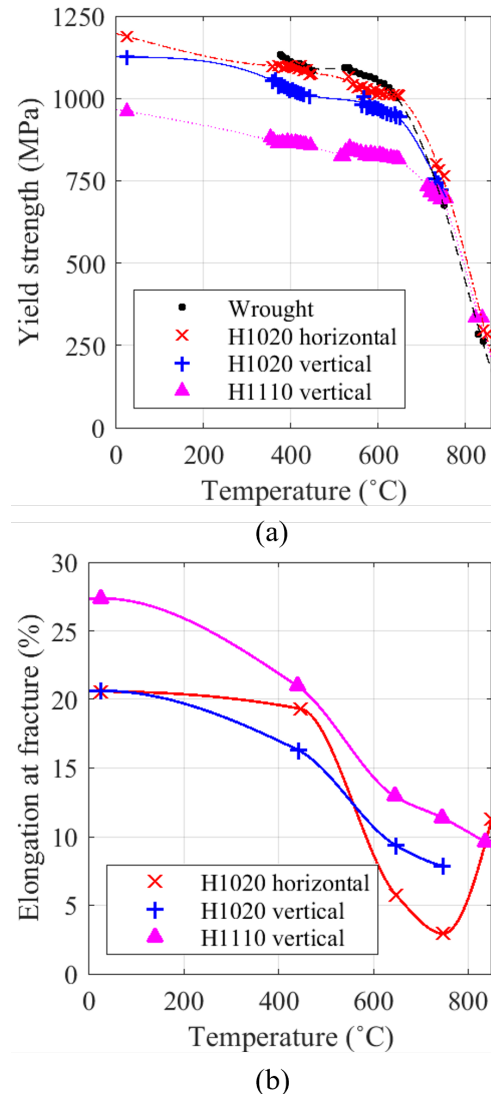

(a)

(b)

Figure 6 Comparative (a) yield strength and (b) elongation as a function of temperature.

Figure 6(b) shows that LPBF IN718 is not exempt from high-temperature embrittlement as indicated by the drop in elongation values after 450 °C. All LPBF specimens perform significantly worse than wrought IN718 at high temperatures where the wrought material achieves an elongation of more than 15.3 % [4] at 650 °C compared to a mere 5.7 % in horizontally printed LPBF specimens. In its current state, the test method also allows for the extraction of other temperature-dependent properties including ultimate tensile strength, Young's modulus, Poison's ratio and hardening coefficients, and with slight adjustment can be used to determine thermal expansion coefficients.

7   Conclusion

This paper highlighted key shortfalls of LPBF IN718, specifically the high degree of embrittlement at high temperatures. Although this embrittlement also occurs in the wrought material, the degree of embrittlement is higher in the LPBF-produced specimens which is detrimental to its potential use in the aerospace industry. This work also showed that the high-temperature properties could be quantified in a specimen-efficient manner using the synchronised Gleeble-DIC-IR technique. Future work is necessary to establish the mechanisms which cause the observed embrittlement.

Acknowledgement

References

[1] M. Perrut, P. Caron, M. Thomas and A. Couret. High temperature materials for aerospace applications: Ni-based superalloys and γ-TiAl alloys. *Comptes Rendus Physique*, 19(8):657–671, 2018.

[2] B. Blakey-Milner, P. Gradl, G. Snedden, M. Brooks, J. Pitot, E. Lopez, M. Leary, F. Berto and A. du Plessis. Metal additive manufacturing in aerospace: A review. *Materials and Design*, 209:110008, 2021.

[3] K. Gruber, W. Stopyra, K. Kobiela, B. Madejski, M. Malicki and T. Kurzynowski. Mechanical properties of Inconel 718 additively manufactured by laser powder bed fusion after industrial high-temperature heat treatment. *Journal of Manufacturing Processes*, 73:642–659, 2022.

[4] Special Metals. INCONEL®Alloy 718. URL `https://www.specialmetals.com/documents/technical-bulletins/inconel/inconel-alloy-718.pdf`

[5] L. Zheng, G. Schmitz, Y. Meng, R. Chellali and R. Schlesiger. Mechanism of Intermediate Temperature Embrittlement of Ni and Ni-based Superalloys. *Critical Reviews in Solid State and Materials Sciences*, 37(3):181–214, 2012.

[6] M. van Rooyen and T.H. Becker. High-temperature tensile property measurements using digital image correlation over a non-uniform temperature field. *Journal of Strain Analysis for Engineering Design*, 53(3):117–129, 2018.

[7] AP&C, Boisbrand, Canada.

[8] E. Uhlmann, J. Düchting, T. Petrat, E. Krohmer, B. Graf and M. Rethmeier. Effects on the distortion of Inconel 718 components along a hybrid laser-based additive manufacturing process chain using laser powder bed fusion and laser metal deposition. *Progress in Additive Manufacturing*, 6:385–394, 2021.

[9] Dynamic Systems Inc, Poestenkill, New York, United States.

[10] Edmund Optics, Barrington, New Jersey, United States.

[11] iDICs. *A Good Practices Guide for Digital Image Correlation*. E.M.C. Jones and M.A. Iadicola, editors. 2018.

[12] Telops, Quebec City, Canada.

[13] Dupli-Color Inc., Cleveland, Ohio, United States.

[14] Fluke, Everett, Washington, United States.

[15] Arduino, Lombardia, Italy.

[16] MatchID, Gent, Belgium.

[17] MathWorks Incorporated, Natick, Massachusetts, United States.

[18] ASTM E21. Standard Test Methods for Elevated Temperature Tension Tests of Metallic Materials. Standard, ASTM International, 2009.